

Highlighting research results by Prof. Gang Liu and coworkers from Xiamen University, China.

Metalla-aromatic loaded magnetic nanoparticles for MRI/photoacoustic imaging-guided cancer phototherapy

We have co-loaded metalla-aromatic agents and a cluster of superparamagnetic iron oxide nanoparticles into a micellar carrier, using a rapid, scalable and versatile approach for dual-modal imaging-guided cancer phototherapy. The prepared nanoformula systems with a photothermal transduction efficiency of 26.6% were also demonstrated as a potential photodynamic sensitizer to generate ROS effectively. Under the guidance of MRI/photoacoustic imaging, the combined photothermal and photodynamic therapy achieved a synergistic anti-tumor effect, significantly improving the therapeutic efficacy both *in vitro* and *in vivo*. The new nanoformula systems also showed good biocompatibility and biosafety, making them a promising candidate for cancer theranostic applications.

As featured in:



See Bin Wang, Haiping Xia, Gang Liu *et al.*, *J. Mater. Chem. B*, 2018, 6, 2528.



Cite this: *J. Mater. Chem. B*, 2018, **6**, 2528

Received 10th August 2017,
Accepted 26th September 2017

DOI: 10.1039/c7tb02145c

rsc.li/materials-b

Metalla-aromatic loaded magnetic nanoparticles for MRI/photoacoustic imaging-guided cancer phototherapy†

Caixia Yang,^{‡ab} Gan Lin,^{‡b} Congqing Zhu,^{‡c} Xin Pang,^b Yang Zhang,^b Xiaoyong Wang,^b Xianglin Li,^a Bin Wang,^{*a} Haiping Xia^{‡b}*^c and Gang Liu^{‡b}*^{bc}

In this study, metalla-aromatic agents (MA) and a cluster of superparamagnetic iron oxide nanoparticles (SPIOs) were loaded inside a micellar carrier (Alkyl-PEI2k-PEG), resulting in MA/SPIOs@Alkyl-PEI2k-PEG nanoparticles (MASAs). The prepared MASAs with a photothermal transduction efficiency of 26.6% were also demonstrated as a potential photodynamic sensitizer to generate ROS effectively. Under the guidance of MRI/photoacoustic imaging, combined photothermal and photodynamic therapy achieved a synergistic anti-tumor effect, significantly improving the therapeutic efficacy of MASAs both *in vitro* and *in vivo*. This work shows that the developed MASAs are a potential theranostic agent for dual-modal imaging-guided cancer phototherapy.

Introduction

Cancer is a major public health problem throughout the whole world.¹ However, clinical cancer therapies are mainly confined to some conventional treatments, such as surgery, radiotherapy or chemotherapy, which still suffer from critical obstacles including radio-resistance and multidrug resistance.² As an emerging treatment modality, photothermal therapy (PTT) has attracted great attention, in which the photothermal agents can convert absorbed light into local heat to selectively kill the surrounding tumour cells. Besides minimal invasiveness against normal tissues, PTT also shows outstanding controllability, high efficiency and selectivity as well as low systemic toxicity. Moreover, it is effective against almost all kinds of

tumours including malignancies, benign tumours and even resistant ones.^{3–5}

So far, a variety of nanomaterials have been applied as photothermal agents for cancer treatment. Among them, inorganic nanomaterials including gold nanostructures,^{6–8} carbon nanotubes,^{9,10} graphene oxide,^{11–13} Pd nanoplates,¹⁴ CuS¹⁵ and transition-metal dichalcogenides¹⁶ have demonstrated great potential in PTT. Despite many achievements, they may be retained in the body for a long time after administration, thus causing safety concerns limiting their translation toward clinical application. Compared with inorganic nanomaterials, near infrared region (NIR)-absorbing organic agents show more rapid clearance from the body and minimized long-term toxicity, and thus represent a promising alternative to inorganic agents in PTT cancer therapy.^{17–20}

However, incomplete ablation involved in PTT will result in tumour re-growth which is an intractable issue to eradicate tumour tissues completely using a single PTT modality. It was recently reported that synergistic therapies by combining PTT with other types of treatment have the potential to fully root out malignant cells, decrease recurrence and bring an overall better treatment efficiency against tumours.^{18,21,22} Photodynamic therapy (PDT) is a clinically approved treatment modality and offers numerous advantages, such as low toxicity to normal tissues, avoidance of intrinsic or acquired resistance, reduced long-term morbidity, *etc.*^{23,24} To date, it has been found that PTT and PDT dual-modality therapies are more effective than PTT or PDT alone owing to the synergistic effects.²⁵

It is a critical issue to obtain detailed information on the disease during therapy. So far, numerous kinds of imaging modality have been applied in imaging-guided cancer therapy to get such detailed information in the disease location. However, each modality has intrinsic limitations as well as its own advantages. To compensate these limitations, multimodal imaging, the combination of different imaging modalities, has been demonstrated to be superior in acquiring more detailed, reliable and accurate information about disease sites.^{26–32} Photoacoustic imaging (PA/PAI) possesses a high spatial resolution of

^a Medical Imaging Research Institute, Binzhou Medical University, Yantai, Shandong 264003, China. E-mail: wangb@bzmc.edu.cn

^b State Key Laboratory of Molecular Vaccinology and Molecular Diagnostics, Center for Molecular Imaging and Translational Medicine, School of Public Health, Xiamen University, Xiamen 361102, China. E-mail: gangliu.cmitm@xmu.edu.cn

^c State Key Laboratory of Physical Chemistry of Solid Surfaces, College of Chemistry and Chemical Engineering, Xiamen University, Xiamen 361005, China. E-mail: hpxia@xmu.edu.cn

† Electronic supplementary information (ESI) available. See DOI: 10.1039/c7tb02145c

‡ These authors contributed equally to this study.

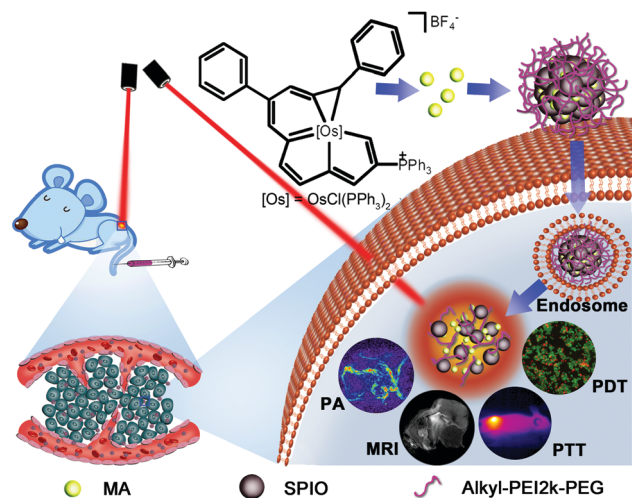


Fig. 1 Schematic of MA-loaded nanoparticles for dual-modal MRI/PA imaging-guided synergistic PTT/PDT cancer therapy.

optical imaging, but insufficient penetration depth due to the limitation of the photoacoustic effect. In contrast, magnetic resonance imaging (MRI) offers excellent spatial resolution and high soft tissue contrast, as well as deep tissue penetration.^{33–37}

Due to the complementary features of these two imaging modalities, PA/MRI dual-modal imaging has shown numerous great advantages in getting access to more accurate and comprehensive information, and thus is a powerful tool in imaging-guided cancer therapy.^{16,38}

In our previous study, we reported a new type of NIR-absorbing organic agent as a photothermal agent, metalla-aromatic complexes.³⁹ These compounds exhibited comparable photothermal heating efficiency with gold nanostructures and carbon nanotubes,^{8,10} both of which are commonly used photothermal agents. In the present study, we also found that these metalla-aromatic compounds can generate reactive oxygen species (ROS) under 630 nm laser irradiation, which makes them a potential candidate for PTT and PDT synergistic therapy (Fig. 1). Metalla-aromatics (MA), along with superparamagnetic iron oxide nanoparticles (SPIOs), were encapsulated into a micellar carrier (Alkyl-PEI2k-PEG) to obtain a MA/SPIOs@Alkyl-PEI2k-PEG drug delivery system (MASAs). Benefiting from the so-called enhanced permeability and retention effect (EPR), the selectivity of MA in the tumour region was obviously enhanced.⁴⁰ Furthermore, these MA and SPIOs contained micellar nanovehicles which also demonstrated great capacity as multi-functional contrast agents for MRI and PA imaging. All of these facts render our developed nanomicelles as a potential theranostic platform for dual-modal imaging-guided PTT/PDT synergistic therapy.

Experimental

Synthesis, purification and characterization of MASAs

Iron oxide (IO) nanocrystals were synthesized by thermal decomposition of iron(III) acetylacetonate. MASAs were prepared according to our previous report with some modifications.⁴¹ Briefly, the IO

nanocrystals were mixed with an amphiphilic polymer (Alkyl-PEI2k-PEG) and MA in chloroform (10 mg IO, 10 mg MA and 5 mg amphiphilic polymer in 1 mL chloroform). The mixed solution was added into distilled water (5 mL) as droplets under sonication. The resulting solution was shaken overnight to evaporate the chloroform. Finally, the nanoparticles were obtained by centrifugation (2000 rpm, 10 min).

The sizes of the MASAs were determined by dynamic light scattering (DLS) (NanoZS 90, Malvern, USA) and transmission electron microscopy (TEM) (Tecnai G2 Spirit BioTwin, FEI, USA). Zeta potentials were determined by a zeta potential analyzer (NanoZS 90, Malvern, USA). The encapsulation efficiency of MA was determined by measuring the amount of unloaded MA in the sediment. The content of Fe was calculated using atomic absorption spectroscopy (AAS).

Phototherapy performances of the MASAs

The photothermal heating effect of the MASAs was determined by irradiating a series of MASA solutions in PBS (pH 7.4) with different MA concentrations from 1 to 100 $\mu\text{g mL}^{-1}$ using a NIR laser (wavelength, 808 nm; power density, 1 W cm^{-2}) for a pre-determined period, and the real-time temperature rises were recorded by a FLIR Ax5 thermal camera.

The photothermal conversion efficiency of the MASAs was measured according to the previously reported method.^{42,43} The photothermal conversion efficiency was calculated using the reported equation. Reactive oxygen species (ROS) measurement was carried out using 2',7'-dichlorodihydrofluorescein (DCFH) as a probe.⁴⁴

Evaluation of the MR/PA imaging capacity of the MASAs

The T_2 relaxivity of the nanoparticles was measured using a 9.4 T MR scanner (Bruker 94/20 USR, Germany) at room temperature as described.⁴¹ T_2 -Weighted MR images were acquired using a fast spin-echo (FSE) sequence with the following parameters: TR/TE = 2500/33 ms (T_2), 256×256 matrices. The value of r_2 was obtained through curve fitting of the $1/T_2$ relaxation time (s^{-1}) vs. the iron concentration (mM Fe). The PA images of the MASAs were acquired using a preclinical PA imaging system (Endra Nexus 128, Ann Arbor, MI) under 800 nm laser with moderate laser energy at $\sim 5 \text{ mJ cm}^{-2}$. The laser maintains a pulse width of 7 ns, and a repetition rate of 20 Hz.

Cell uptake assay

Before experiments, SCC-7 cells were grown in DMEM medium containing 10% fetal bovine serum (FBS) and 1% streptomycin/ampicillin at 37 °C with 5% CO_2 . Perls staining (neutral red method) was employed to visualize the internalization of the MASAs. Images were obtained using an inverted fluorescence microscope (Nikon, Ti-U).

Cellular single oxygen detection

A reactive oxygen species assay kit (DCFH-DA) was used to evaluate the production of singlet oxygen in SCC-7 cells. After SCC-7 cells were incubated with MASA sample solutions of different concentrations (MA concentration: 0, 1, 5, 10, 30, 50,

100 $\mu\text{g ml}^{-1}$) for 6 h, the medium was replaced with fresh DMEM medium (without FBS) containing 10 μM DCFH-DA and further incubated for 20 min. After the incubation, the cells were washed 3 times with fresh medium to remove the redundant DCFH-DA and irradiated with a 630 nm NIR laser (power density: 130 mW cm^{-2}) for 5 min. Finally, the cells were collected to determine the fluorescence intensity of DCF in the cells using a multimode reader (Victor 3 V).

PTT/PDT cell killing assay

SCC-7 cells (1×10^4) were seeded on 96-well plates and incubated with MASA samples (MA concentration: 1, 5, 10, 30, 50 $\mu\text{g ml}^{-1}$) for 6 h, and then the medium was replaced with fresh medium. In the PTT group, the cells were irradiated with an 808 nm NIR laser (power density, 1 W cm^{-2}) for 10 min, while the cells in the PDT group were irradiated with a 630 nm NIR laser (power density, 130 mW cm^{-2}) for 5 min. The untreated cells were set as the control group. In addition, the cells in the PTT/PDT group were first irradiated with an 808 nm NIR laser for 10 min, and then treated with a 630 nm NIR laser for 5 min. The power densities of 808 nm and 630 nm were 1 W cm^{-2} and 130 mW cm^{-2} respectively. After the irradiation, the cells were incubated overnight and methylthiazolyl tetrazolium (MTT) assays were carried out to evaluate the cell viability.

To further demonstrate that cell death was caused by the produced ROS, we incubated the cells with 2 mM *N*-acetyl-L-cysteine (NAC, sigma, A9165) for 30 min.⁴⁵ After irradiation at 630 nm for 5 min, an MTT assay was performed to determine the cell viability.

The cell death caused by the synergistic PTT/PDT effect was also confirmed by Calcein AM/PI staining. The cells were grown in DMEM medium and incubated with MASAs (MA concentration: 50 $\mu\text{g ml}^{-1}$) for 6 h. After irradiation at 808 nm and 630 nm, the cells were stained with Calcein-AM (AM, 2 μM) and propidium iodide (PI, 4 μM) for 30 min. Images were acquired using an inverted fluorescence microscope (Nikon, Ti-U).

In vitro magnetic resonance imaging

The SCC-7 cells (5×10^5) were seeded in 6-well plates and incubated with MASAs with different Fe concentrations (1, 5, 10, 30 $\mu\text{g mL}^{-1}$) for 24 h. The cells were then harvested by trypsinization and re-dispersed in 1% agarose gel for MRI analysis. The T_2 relaxation measurements were performed using a 9.4 T MRI scanner (Bruker 94/20 USR, Germany) with a 4 cm volume coil and using spin-echo imaging sequences. Images were acquired using the following parameters: repetition time (TR) = 2500 ms, echo time (TE) = 30 ms, acquisition matrix = 256 \times 256 mm, and slice thickness = 1 mm. The signal intensities of each sample were acquired by using the analysis program provided by the MRI scanner. And the T_2 signal intensity of the treated cells was displayed as a percentile relative to the untreated ones.

Animal models

Animal studies were performed according to a protocol approved by Xiamen University Laboratory Animal Center. Animal models

were established by subcutaneous injection of 5×10^6 SCC-7 cells in 100 μL serum-free DMEM medium into the dorsal part of the mice.

In vivo MR/PA imaging

In vivo MRI studies were performed using a 9.4 T imaging system (Bruker 94/20 USR, Germany) by using a mouse coil (Bruker) for transmission and reception of the signal. A multi-section T_2 -weighted FSE sequence (TR = 2500 ms; TE = 33 ms; FOV = 40 mm \times 40 mm; slice thickness 1 mm; flip angle 180) was used for all of our studies. MRI scans were performed before and 3, 6, 12 and 24 h after contrast agent administration at a dose of 6 mg (Fe) kg^{-1} body weight. Signal intensity (SI) was measured at pre-determined time points, and the relative SI was displayed as a percentile relative to the SI before injection.

In vivo PA images were acquired using a preclinical PA imaging system (Endra Nexus 128, Ann Arbor, MI) under an 800 nm laser with a moderate laser energy of $\sim 5 \text{ mJ cm}^{-2}$. The laser maintains a pulse width of 7 ns, and a repetition rate of 20 Hz. Isoflurane was used to maintain the anesthesia of the mice, and the water heating system of the Endra Nexus 128 kept the mice warm. The tumour PA images were acquired before and 3, 6, 12 and 24 h after intravenous injection of MASAs (MA: 20 mg kg^{-1}). The photoacoustic signal intensity was evaluated by analyzing the region of interest (ROI).

In vivo PTT/PDT synergistic therapy

When the tumours reached $\sim 40 \text{ mm}^3$ (about 7 days after transplantation), the animals were randomly divided into 6 groups ($n = 3$): (a) PBS administered only; (b) PBS administered and 808/630 nm laser irradiated; (c) MASAs administered only; (d) MASAs administered and 808 nm laser irradiated (PTT group); (e) MASAs administered and 630 nm laser irradiated (PDT group); and (f) MASAs administered and 808/630 nm laser irradiated (PTT/PDT synergistic therapy group).

In the PTT group, the tumours were exposed to an 808 nm laser of power density 1 W cm^{-2} for 10 min. Meanwhile, the ones in the PDT group were exposed to a 630 nm laser of power density 130 mW cm^{-2} for 5 min. The temperature rise in the tumour tissues during the PTT was recorded by an IR camera (FLIR Ax5) in real time. The tumour volumes of each group were measured every other day to evaluate the anticancer efficacy for 14 days. It was calculated as follows: $V = L \times W^2/2$, where L is the tumour dimension at the longest point, and W is the tumour dimension at the widest point. The tumour volumes are normalized against the original volumes at day 0. The body weight of the mice also measured every other day to observe the acute toxicity of the MASAs.

Ex vivo histological staining

One day after PTT/PDT treatment, tumour tissues were collected and fixed in a 4% formaldehyde solution followed by hematoxylin and eosin (H&E) staining. The major organs of the mice were collected 30 days post the injection of MASAs (MA: 7.5 mg kg^{-1}). Subsequently, these organs were fixed in 4% formaldehyde solution, processed into paraffin, sectioned at 8-micron thickness,

stained with H&E and examined by an inverted fluorescence microscope (Nikon, Ti-U).

Statistical analysis

The data were statistically analyzed by Student's *t*-test and $P < 0.05$ was considered statistically significant.

Results and discussion

Preparation and characterization

The multifunctional nanoparticles were formed through the self-assembly of MA and SPIOs with amphiphilic polymer (Fig. 2A and B). Fig. S1 (ESI[†]) shows the results of UV-visible spectroscopy in water. The encapsulation efficiencies were 66% and 79% for MA and SPIO, respectively. The results of DLS indicated that the sizes of these nanoparticles were around 85 nm (Fig. 2C). Such small hydrodynamic size is favourable for the EPR effect to increase the accumulation of nanoparticles in tumour sites.⁴⁰ Transmission electron microscopy (TEM) data showed that these nanoparticles possess a uniform size distribution (Fig. 2D). As shown in Fig. 2E, the multifunctional nanoparticles were stable at room temperature and no sediment was observed after six days. It should be noticed that the SPIOs formed cluster structures in the core of the nanoparticles, which resulted in a significantly high r_2 value ($295.1 \text{ Fe mM}^{-1} \text{ s}^{-1}$) (Fig. 2F), making the MASAs a great MRI T_2 contrast agent.⁴⁶ As expected, the as-prepared nanoparticles also showed enhanced PA signal intensity with an increase in MA concentration (Fig. 2G).

Phototherapy behaviours of the nanoparticles

One critical feature of PTT agents is to effectively convert the absorbed NIR light to heat, which can be applied in tumour thermal ablation.^{47–50} To investigate the photothermal heating efficiency of the MASAs, sample solutions with different concentrations of MA were exposed to an 808 nm laser (Fig. 3A).

It was found that the photothermal effect of the nanoparticles displayed a concentration-dependent manner and the temperature of the solution with the highest MA concentration ($300 \mu\text{g mL}^{-1}$) rose rapidly by $51.8 \text{ }^\circ\text{C}$. In contrast, the temperature rise of water during the irradiation was negligible (from $27.5 \text{ }^\circ\text{C}$ to $30.2 \text{ }^\circ\text{C}$). Although SPIO nanoclusters could elevate the temperature slightly upon laser irradiation, it was found that the photothermal heating effect of the MASAs was mainly caused by the MA (Fig. S2, ESI[†]).

The photothermal conversion efficiency (η) is one important parameter for characterizing the efficiency of photothermal heating effects. It was calculated using the reported method.^{42,43} The τ s was determined as 87.2 s from the linear time data *versus* $-\ln(\theta)$ obtained from the cooling stage (Fig. 3B). By using the reported equation, the η value of the MASAs was found to be about 26.6%, which was comparable with that of Au nanorods and Cu_2S_5 nanocrystals, both of which are commonly investigated photothermal agents.^{43,51} As photothermal stability greatly affected the PTT efficiency, we further tested the photothermal stability of the nanoparticles by irradiating samples with an

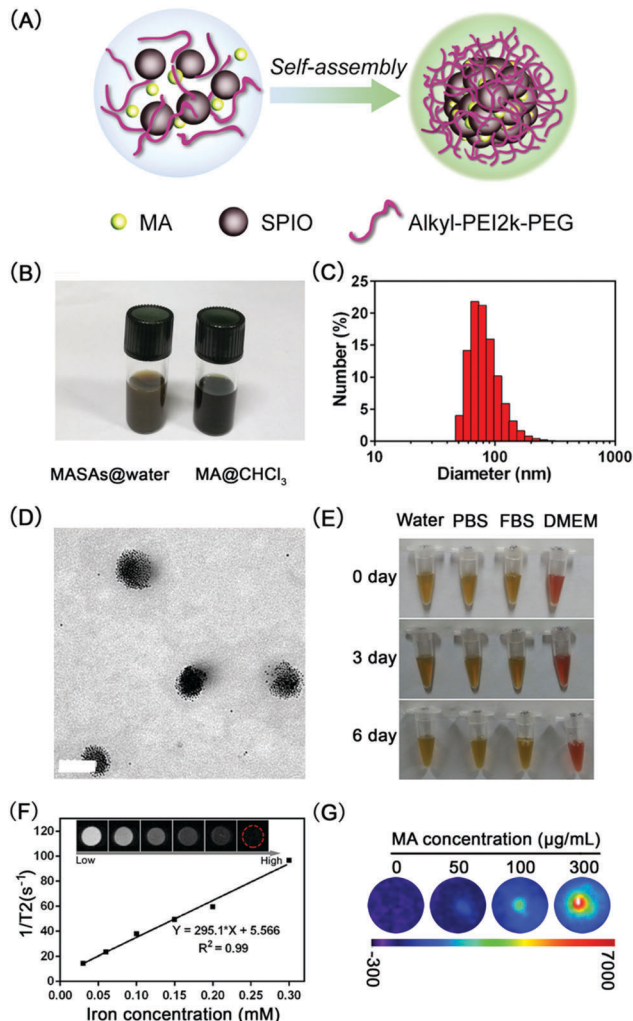


Fig. 2 Nanoparticle preparation and characterization. (A) Schematic illustration of nanoparticle preparation. Multifunctional nanoparticles were obtained by assembly of MA and SPIO with PEGylated cationic amphiphile (Alkyl-PEI2k-PEG). (B) Image of an MASA aqueous solution and free MA in CHCl_3 . (C) Dynamic light scattering characterization of MASAs. (D) TEM image of MASAs, scale bar: 100 nm. (E) Photographs of MASA samples incubated in water, PBS, FBS and DMEM. (F) T_2 relaxation rate ($1/T_2, \text{ s}^{-1}$) as a function of Fe concentration (mM) for MASAs at 9.4 T. (G) PAI signals of MASAs with different MA concentrations ($0, 50, 100, 300 \mu\text{g mL}^{-1}$).

808 nm laser for 5 min followed by switching the laser off, and repeating the laser on-and-off process for several cycles (Fig. 3C). It was observed that the temperature increase in the samples (MA concentration: $100 \mu\text{g mL}^{-1}$) remained very stable even after 5 repeated laser on-and-off cycles, indicating no obvious loss of photothermal heating capacity during the laser irradiation. The excellent photothermal stability was also confirmed by the results of UV-vis spectroscopy (Fig. S3, ESI[†]). In contrast, the temperature increase in the sample containing indocyanine green (ICG), which is one of the commonly used photothermal agents, just remained 37.6% of that in the first cycle at the same concentration (Fig. S4, ESI[†]). These results demonstrated the great photothermal conversion efficiency and excellent photothermal stability, rendering MASAs a promising photothermal agent for PTT.

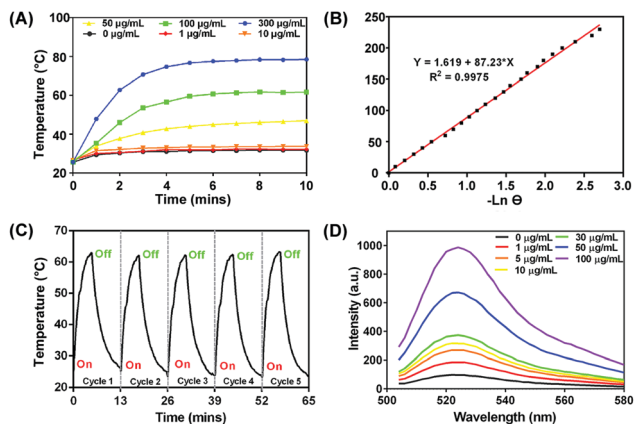


Fig. 3 MASA performances in PTT, PDT, MRI and PAI. (A) Temperature increase curves of MASA samples with different MA concentrations (0, 1, 10, 50, 100, 300 $\mu\text{g mL}^{-1}$) irradiated with an 808 nm laser (1 W cm^{-2} , 10 min). (B) Determination of photothermal conversion efficiency. (C) Investigation of the photostability of MASAs containing $100 \mu\text{g mL}^{-1}$ MA. (D) Assessment of ROS generation of MASAs under a 630 nm laser (130 mW cm^{-2} , 5 min).

The potential of MASAs applied in PDT was also explored. Since ROS generation played a critical role in determining the therapeutic effect of PDT, the ability of MASAs to generate ROS was therefore investigated.⁴⁴ Fig. 3D showed that the fluorescence of DCFH rises with increasing concentration of mixed nanoparticles, indicating that MASAs had the ability to generate ROS under a 630 nm laser. In addition, the UV-vis spectrum (Fig. S3, ESI[†]) revealed no obvious change in the spectrum, suggesting a good photostability of MASAs during the PDT. Considering the good performances in photothermal heating as well as ROS generation, our multifunctional nanoparticles can be regarded as a suitable platform for PTT/PDT synergistic therapy.

In vitro behaviors

Before analysing the *in vitro* photo-therapeutic efficacy of the nanoparticles, the dark cytotoxicity of free MA and MASAs was measured in two different cell lines, 4T1 and U87 cells. It was found that the free MA induced obvious cytotoxicity even at relatively low concentration ($10 \mu\text{g mL}^{-1}$), and the cell viability decreased to around 50% at $100 \mu\text{g mL}^{-1}$ (Fig. S5, ESI[†]). In contrast, the MA containing nanoparticles showed excellent biocompatibility and did not induce obvious cytotoxicity (Fig. S6, ESI[†]).

As mentioned above, the r_2 value of MASAs was determined as $295.1 \text{ Fe mM}^{-1} \text{ s}^{-1}$, which was much higher than that of the commercial T_2 contrast agent Feridex ($98.3 \text{ Fe mM}^{-1} \text{ s}^{-1}$). Generally, a higher r_2 value brings a better contrast agent for T_2 MRI imaging. Under a 9.4 T MRI scanner, the nanoparticle treated cells displayed a significant decrease in signal intensity compared with the control one (Fig. 4A). The cellular internalization of MASAs was confirmed by Prussian blue staining (Fig. S7, ESI[†]). SPIO-based MRI contrast agents had the ability to shorten the spin-spin relaxation time, bringing hypointensities in T_2 -weighted images. Thus taking their performance in MRI and

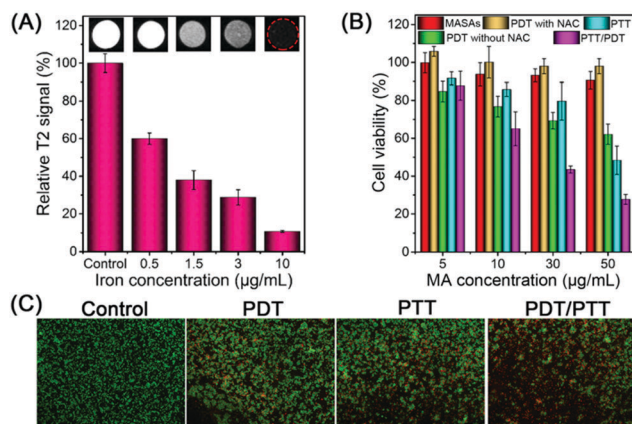


Fig. 4 MASA MRI performances and phototherapy efficiency on SCC-7 cells. (A) *In vitro* MRI signals of SCC-7 cancer cells treated with different concentrations of MASAs. (B) Cell viabilities after various kinds of therapy modalities at different concentrations of MASAs. Cell viabilities were investigated by standard MTT assays. (C) Fluorescence images of AM/PI stained cells after different therapies, scale bar: 200 μm .

PA into account, MASAs show great potential to track the loaded agents during delivery.

As shown in Fig. 4B, the cell viabilities in the PDT, PTT and PTT/PDT groups decreased with an increase in MA concentration. Considering the negligible dark cytotoxicity of MASAs, the improved efficiency was attributed to the laser which can induce rapid generation of heat and ROS from MASAs in the PTT and PDT groups respectively. It was also noticed that the photo-therapeutic efficacy of MASAs in PTT/PDT was significantly higher than that in PDT alone and or PTT alone. At the highest MA concentration of $50 \mu\text{g mL}^{-1}$, the cell viability in the PTT/PDT group decreased to 27%, while 48% and 62% of cells were alive in the PTT and PDT groups, respectively (Fig. 4B).

To investigate the in-depth mechanism of cell death in the PDT group, nanoparticle-treated SCC-7 cells were incubated with *N*-acetyl-L-cysteine (NAC) before laser irradiation. It has been reported that NAC is an effective ROS scavenger and protects SCC-7 cells from ROS damage.⁴⁵ As shown in Fig. 4B, the viability in the group without NAC decreased with an increase in MA concentration. However, MASAs did not induce obvious cytotoxicity with laser irradiation when the cells were treated with NAC. There were no significant differences ($P > 0.05$) between the viabilities of cells in the NAC-treated group and in the control group, suggesting that cell death in the PDT group was mainly caused by the generation of ROS. The photo-therapeutic effects of MASAs on SCC-7 cells were also confirmed by calcein AM and propidium iodide (PI) co-staining (Fig. 4C), indicating an enhanced cancer cell killing effect of synergistic PTT/PDT therapy.

In vivo MR/PA imaging and phototherapy

One important function of theranostic nanoplatforms is to image the delivery process and obtain information about drug accumulation in the disease region.^{52–54} To get such information, *in vivo* MRI and PA imaging was performed on SCC-7 tumour bearing mice when the tumour size reached 100 mm^3 in our

study. Before and after intravenous injection of MASAs, we performed MRI and PA imaging to confirm the MASA accumulation in the tumour areas. As shown in Fig. 5A, the T_2 value of the tumour section reached the lowest at 6 h post injection and then increased slightly, suggesting the highest accumulation of MASAs at the 6 h time point. The photoacoustic images (Fig. 5B) showed the vasculatures of the tumours, which was displayed with transverse maximum intensity projection (MIP). The post-injection scan images show more blood vessels and remarkably increased contrast compared to that before injection. Identical regions of interest (ROI) were selected in each image to further

analyse the PA signal intensity. And the normalized PA intensity curve showed that the tumour signal intensity reached the highest value at 6 h post injection, which was consistent with the results of MRI.

Within 5 min, the temperature of the irradiated tumour region with MASA injection increased to about 52 °C rapidly (Fig. 5C and D). Meanwhile, there was negligible temperature increase in regions without laser irradiation. In contrast, the temperature of the tumour region in the PBS group just showed a limited temperature increase (to 40 °C) when exposed to irradiation. All these results demonstrated the accumulation of

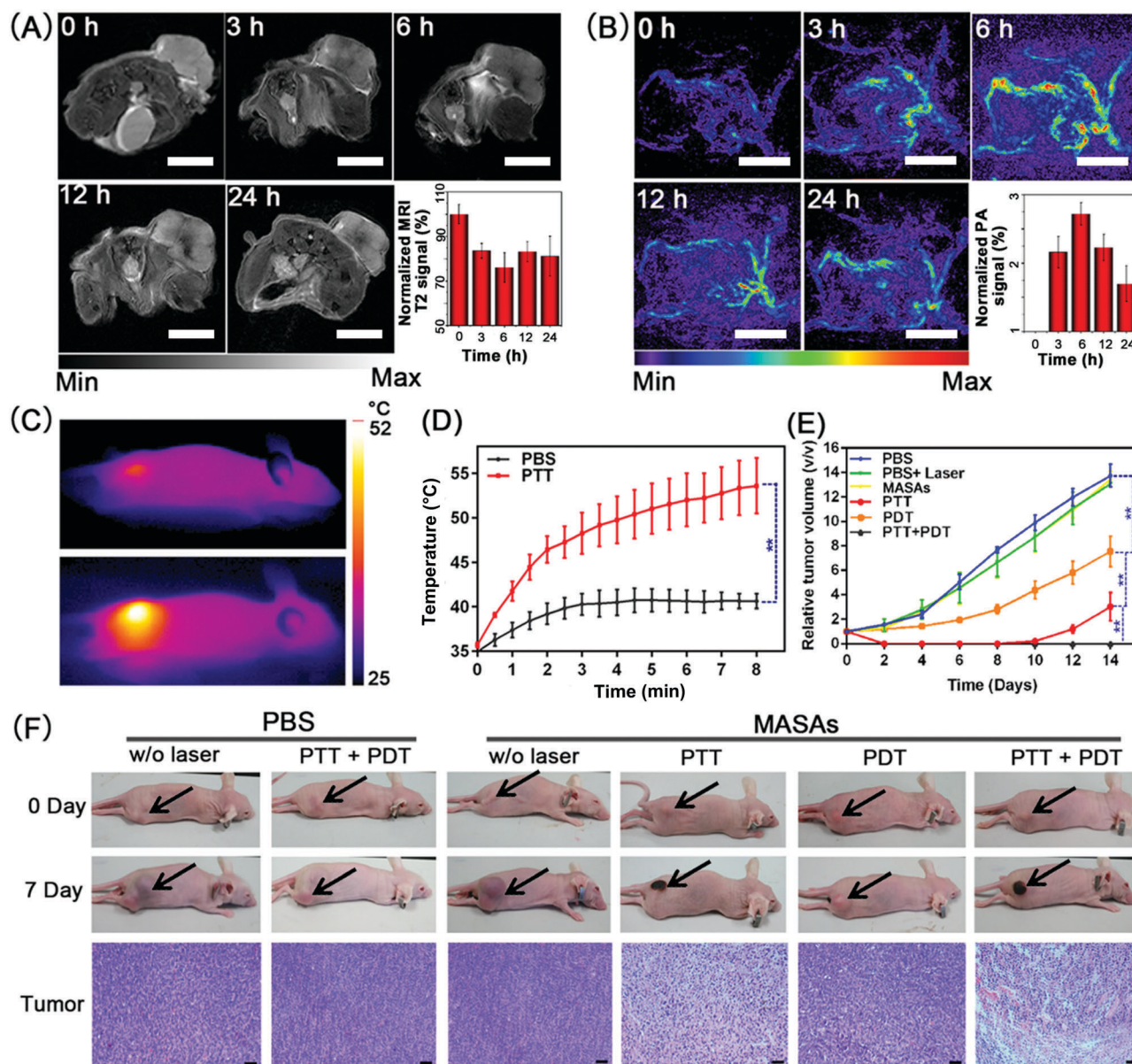


Fig. 5 *In vivo* MASA MR/PA imaging and phototherapy efficiency evaluation in SCC-7 tumour-bearing mice. (A) *In vivo* MR imaging at different time points (0, 3, 6, 12, 24 h), scale bar: 1 cm; inset is the normalized reduction of MRI signals in the tumour region at pre-determined time points. (B) *In vivo* PA imaging at different time points; inset is normalized PAI signal enhancements in the tumour area at pre-determined time points, scale bar: 0.5 cm. (C) Infrared thermographic maps of SCC-7 tumour-bearing mice treated with PBS or MASAs under laser irradiation. (D) Temperature increase curves of the irradiated area of tumour-bearing mice with PBS or MASA injection (*i.v.*). (E) Tumour growth curves and (F) representative photographs of mice bearing SCC-7 tumours and H&E staining of the tumour region after different therapies. The black arrows show the position of the tumours. Scale bar: 50 μ m.

MASAs in the tumour region, which had been confirmed by the data of MRI and PA imaging.

The growth rates of the tumours were also recorded to verify the *in vivo* therapeutic efficacy of MASAs for 14 days (Fig. 5E). The tumour growths in the PTT, PDT, and PTT/PDT treatment groups showed significant delay, when compared to the PBS alone group ($P < 0.01$). The MASAs alone did not induce any effect in inhibiting tumour growth. Meanwhile, PBS plus 808/630 nm laser irradiation also failed to cause a delay in tumour growth. It was noted that the therapeutic effect of the nanoparticles in the PTT group was slightly higher than that in the PDT group. The main reason may be due to the shallower tissue penetration depth of the 630 nm laser compared with 808 nm, resulting in insufficient generation of ROS from MA and subsequent lower suppression efficiency in tumour growth. In addition, there were tumour recurrences in the PTT group after 10 days, which may be due to the incomplete ablation of tumour tissues. In marked contrast, the tumour size in the PTT/PDT group was maintained at 0% during the therapy (day 2 to day 14). The enhanced improvement of therapeutic effect demonstrated the advantages of the synergistic PTT/PDT over a single modality treatment alone.

To further study the phototherapy effect of MASAs, H&E staining of tumour tissue sections was performed 24 h after treatment (Fig. 5F). The tumour tissues treated with PBS, nanoparticles and PBS plus laser irradiation showed indiscernible necrosis with infiltrating tumour cells and pleomorphic nuclei. The tumour tissues remained undamaged and intact, indicating the minimal dark toxicity of MASAs and negligible damage of the laser alone. In contrast, there was notable necrosis, decreased tumour tissue intensity and disturbed tumour architecture in the three phototherapy groups, especially in the PTT/PDT group. Karyopyknosis was common in the PTT/PDT combined treatment group, consistent with the tumour growth rates.

The long-term toxicity of the MASAs was assessed by monitoring the changes in body weight and major organ H&E staining. During the whole therapy, there were no significant body weight changes in the treated mice (Fig. S8, ESI†). The major organs from SCC-7 tumour-bearing nude mice of each group were also analysed. No visible organ damage was detected in the stained slices (Fig. S9, ESI†), suggesting that MASAs did not induce general toxic side effects in mice for 2 weeks. The typical biodistribution and clearance of nanoparticles depend on their size and surface characteristics, predominantly by action of the liver and spleen macrophages. It is noteworthy to mention that the metallaromatic agent MA exhibits excellent thermodynamic stability according to our previous research.^{39,55,56} The metallic element osmium in MA might be eliminated through urine/feces and we are now working on the biodistribution of MASAs used as intravenous theranostics for a better toxicological understanding of MASAs.

Conclusions

In summary, MASAs were successfully synthesized and used for MRI/PA dual-modal imaging-guided PTT/PDT synergistic

tumour therapy. The enhanced stability in aqueous solution, high photothermal-conversion efficiency and photothermal stability offer the nanoplatform powerful capabilities for highly effective PTT. The great ability of ROS generation further facilitates MA as a promising photosensitizer for PDT. Combined with effective photothermal and photodynamic activities, the tumour recurrence rate was greatly reduced after PTT/PDT therapy. Preferential accumulation of the MASAs around the tumour tissue was demonstrated with MRI/PA dual-modal imaging. Finally, the MASAs showed good biocompatibility and biosafety, making them a promising candidate for cancer theranostic applications.

Conflicts of interest

There are no conflicts to declare.

Acknowledgements

This work is supported by the Major State Basic Research Development Program of China (Grant no. 2017YFA0205201, 2014CB744503, and 2013CB733802), the National Natural Science Foundation of China (NSFC) (Grant no. 81422023, 81371596, 61327001, and U1505221), the Science Foundation of Fujian Province (2014Y2004), the Program for New Century Excellent Talents in University (NCET-13-0502), and the Fundamental Research Funds for the Central Universities, China (20720150206 and 20720150141).

Notes and references

- 1 R. Siegel, J. Ma, Z. Zou and A. Jemal, *Ca-Cancer J. Clin.*, 2014, **64**, 9–29.
- 2 G. Lin, P. Mi, C. Chu, J. Zhang and G. Liu, *Adv. Sci.*, 2016, **3**, 1600134.
- 3 Q. Tian, J. Hu, Y. Zhu, R. Zou, Z. Chen, S. Yang, R. Li, Q. Su, Y. Han and X. Liu, *J. Am. Chem. Soc.*, 2013, **135**, 8571–8577.
- 4 C. M. Hu and L. Zhang, *Biochem. Pharmacol.*, 2012, **83**, 1104–1111.
- 5 D. Zhu, M. Liu, X. Liu, Y. Liu, P. N. Prasad and M. T. Swihart, *J. Mater. Chem. B*, 2017, **5**, 4934–4942.
- 6 R. He, Y. C. Wang, X. Wang, Z. Wang, G. Liu, W. Zhou, L. Wen, Q. Li, X. Wang, X. Chen, J. Zeng and J. G. Hou, *Nat. Commun.*, 2014, **5**, 4327.
- 7 L. Nie, S. Wang, X. Wang, P. Rong, Y. Ma, G. Liu, P. Huang, G. Lu and X. Chen, *Small*, 2014, **10**, 1585–1593.
- 8 J. Hu, X. Zhu, H. Li, Z. Zhao, X. Chi, G. Huang, D. Huang, G. Liu, X. Wang and J. Gao, *Theranostics*, 2014, **4**, 534–545.
- 9 R. Singh and S. V. Torti, *Adv. Drug Delivery Rev.*, 2013, **65**, 2045–2060.
- 10 R. Gulotty, M. Castellino, P. Jagdale, A. Tagliaferro and A. A. Balandin, *ACS Nano*, 2013, **7**, 5114–5121.
- 11 K. Yang, J. Wan, S. Zhang, B. Tian, Y. Zhang and Z. Liu, *Biomaterials*, 2012, **33**, 2206–2214.
- 12 A. Sahu, W. I. Choi, J. H. Lee and G. Tae, *Biomaterials*, 2013, **34**, 6239–6248.

- 13 X. Shi, H. Gong, Y. Li, C. Wang, L. Cheng and Z. Liu, *Biomaterials*, 2013, **34**, 4786–4793.
- 14 M. Chen, S. Tang, Z. Guo, X. Wang, S. Mo, X. Huang, G. Liu and N. Zheng, *Adv. Mater.*, 2014, **26**, 8210–8216.
- 15 Z. Wang, P. Huang, O. Jacobson, Z. Wang, Y. Liu, L. Lin, J. Lin, N. Lu, H. Zhang, R. Tian, G. Niu, G. Liu and X. Chen, *ACS Nano*, 2016, **10**, 3453–3460.
- 16 X. R. Song, X. Wang, S. X. Yu, J. Cao, S. H. Li, J. Li, G. Liu, H. H. Yang and X. Chen, *Adv. Mater.*, 2015, **27**, 3285–3291.
- 17 M. Guo, H. Mao, Y. Li, A. Zhu, H. He, H. Yang, Y. Wang, X. Tian, C. Ge, Q. Peng, X. Wang, X. Yang, X. Chen, G. Liu and H. Chen, *Biomaterials*, 2014, **35**, 4656–4666.
- 18 Z. Wan, H. Mao, M. Guo, Y. Li, A. Zhu, H. Yang, H. He, J. Shen, L. Zhou, Z. Jiang, C. Ge, X. Chen, X. Yang, G. Liu and H. Chen, *Theranostics*, 2014, **4**, 399–411.
- 19 X. Song, H. Gong, T. Liu, L. Cheng, C. Wang, X. Sun, C. Liang and Z. Liu, *Small*, 2014, **10**, 4362–4370.
- 20 L. Hou, J. Fang, W. Wang, Z. Xie, D. Dong and N. Zhang, *J. Mater. Chem. B*, 2017, **5**, 3348–3354.
- 21 C. He, S. Jiang, H. Jin, S. Chen, G. Lin, H. Yao, X. Wang, P. Mi, Z. Ji, Y. Lin, Z. Lin and G. Liu, *Biomaterials*, 2016, **83**, 102–114.
- 22 L. Cheng, C. Wang, L. Feng, K. Yang and Z. Liu, *Chem. Rev.*, 2014, **114**, 10869–10939.
- 23 Z. Zhen, W. Tang, C. Guo, H. Chen, X. Lin, G. Liu, B. Fei, X. Chen, B. Xu and J. Xie, *ACS Nano*, 2013, **7**, 6988–6996.
- 24 Z. Zhen, W. Tang, Y. J. Chuang, T. Todd, W. Zhang, X. Lin, G. Niu, G. Liu, L. Wang, Z. Pan, X. Chen and J. Xie, *ACS Nano*, 2014, **8**, 6004–6013.
- 25 C. Huang, C. Chu, X. Wang, H. Lin, J. Wang, Y. Zeng, W. Zhu, Y. J. Wang and G. Liu, *Biomater. Sci.*, 2017, **5**, 1512–1516.
- 26 L. Cheng, J. Liu, X. Gu, H. Gong, X. Shi, T. Liu, C. Wang, X. Wang, G. Liu, H. Xing, W. Bu, B. Sun and Z. Liu, *Adv. Mater.*, 2014, **26**, 1886–1893.
- 27 X. Song, H. Gong, S. Yin, L. Cheng, C. Wang, Z. Li, Y. Li, X. Wang, G. Liu and Z. Liu, *Adv. Funct. Mater.*, 2014, **24**, 1194–1201.
- 28 W. Cai, H. Gao, C. Chu, X. Wang, J. Wang, P. Zhang, G. Lin, W. Li, G. Liu and X. Chen, *ACS Appl. Mater. Interfaces*, 2017, **9**, 2040–2051.
- 29 C. Liang, S. Diao, C. Wang, H. Gong, T. Liu, G. Hong, X. Shi, H. Dai and Z. Liu, *Adv. Mater.*, 2014, **26**, 5646–5652.
- 30 S. Wen, L. Zhao, Q. Zhao, D. Li, C. Liu, Z. Yu, M. Shen, J. P. Majoral, S. Mignani and J. Zhao, *J. Mater. Chem. B*, 2017, **5**, 3810–3815.
- 31 Z. Li, H. Ling, Y. Zhang, Y. Zhao, H. Yang and G. Han, *Nano Res.*, 2017, **10**, 1840–1846.
- 32 Z. Li, Y. Zhang, X. Wu, L. Huang, D. Li, W. Fan and G. Han, *J. Am. Chem. Soc.*, 2015, **137**, 5304–5307.
- 33 Y. Zeng, L. Wang, Z. Zhou, X. Wang, Y. Zhang, J. Wang, P. Mi, G. Liu and L. Zhou, *Biomater. Sci.*, 2016, **5**, 50–56.
- 34 Z. Zhou, R. Tian, Z. Wang, Z. Yang, Y. Liu, G. Liu, R. Wang, J. Gao, J. Song, L. Nie and X. Chen, *Nat. Commun.*, 2017, **8**, 15468.
- 35 H. Liu, J. Zhang, X. Chen, X. S. Du, J. L. Zhang, G. Liu and W. G. Zhang, *Nanoscale*, 2016, **8**, 7808–7826.
- 36 Y. Liu, B. W. Muir, L. J. Waddington, T. M. Hinton, B. A. Moffat, X. Hao, J. Qiu and T. C. Hughes, *Biomacromolecules*, 2015, **16**, 790–797.
- 37 H. Liu, X. Chen, W. Xue, C. Chu, Y. Liu, H. Tong, X. Du, T. Xie, G. Liu and W. Zhang, *Int. J. Nanomed.*, 2016, **11**, 5099–5108.
- 38 T. Fu, Y. Chen, J. Hao, X. Wang, G. Liu, Y. Li, Z. Liu and L. Cheng, *Nanoscale*, 2015, **7**, 20757–20768.
- 39 C. Zhu, C. Yang, Y. Wang, G. Lin, Y. Yang, X. Wang, J. Zhu, X. Chen, X. Lu, G. Liu and H. Xia, *Sci. Adv.*, 2016, **2**, e1601031.
- 40 K. Yang, S. Zhang, G. Zhang, X. Sun, S. T. Lee and Z. Liu, *Nano Lett.*, 2010, **10**, 3318–3323.
- 41 G. Liu, Z. Wang, J. Lu, C. Xia, F. Gao, Q. Gong, B. Song, X. Zhao, X. Shuai, X. Chen, H. Ai and Z. Gu, *Biomaterials*, 2011, **32**, 528–537.
- 42 Z. Li, J. Liu, Y. Hu, K. A. Howard, Z. Li, X. Fan, M. Chang, Y. Sun, F. Besenbacher, C. Chen and M. Yu, *ACS Nano*, 2016, **10**, 9646–9658.
- 43 Q. Tian, F. Jiang, R. Zou, Q. Liu, Z. Chen, M. Zhu, S. Yang, J. Wang, J. Wang and J. Hu, *ACS Nano*, 2011, **5**, 9761–9771.
- 44 L. Bourre, S. Thibaut, A. Briffaud, N. Rousset, S. Eleouet, Y. Lajat and T. Patrice, *J. Photochem. Photobiol., B*, 2002, **67**, 23–31.
- 45 J. Tian, L. Ding, H. J. Xu, Z. Shen, H. Ju, L. Jia, L. Bao and J. S. Yu, *J. Am. Chem. Soc.*, 2013, **135**, 18850–18858.
- 46 D. E. Lee, H. Koo, I. C. Sun, J. H. Ryu, K. Kim and I. C. Kwon, *Chem. Soc. Rev.*, 2012, **41**, 2656–2672.
- 47 S. Bhana, G. Lin, L. Wang, H. Starring, S. R. Mishra, G. Liu and X. Huang, *ACS Appl. Mater. Interfaces*, 2015, **7**, 11637–11647.
- 48 L. Cheng, H. Gong, W. Zhu, J. Liu, X. Wang, G. Liu and Z. Liu, *Biomaterials*, 2014, **35**, 9844–9852.
- 49 X. R. Song, S. X. Yu, G. X. Jin, X. Wang, J. Chen, J. Li, G. Liu and H. H. Yang, *Small*, 2016, **12**, 1506–1513.
- 50 Y. Wang, K. Wang, J. Zhao, X. Liu, J. Bu, X. Yan and R. Huang, *J. Am. Chem. Soc.*, 2013, **135**, 4799–4804.
- 51 R. Mooney, L. Roma, D. Zhao, D. Van Haute, E. Garcia, S. U. Kim, A. J. Annala, K. S. Aboody and J. M. Berlin, *ACS Nano*, 2014, **8**, 12450–12460.
- 52 J. Wang, P. Mi, G. Lin, Y. X. Wang, G. Liu and X. Chen, *Adv. Drug Delivery Rev.*, 2016, **104**, 44–60.
- 53 X. Wang, Z. Zhou, Z. Wang, Y. Xue, Y. Zeng, J. Gao, L. Zhu, X. Zhang, G. Liu and X. Chen, *Nanoscale*, 2013, **5**, 8098–8104.
- 54 K. Yang, L. Hu, X. Ma, S. Ye, L. Cheng, X. Shi, C. Li, Y. Li and Z. Liu, *Adv. Mater.*, 2012, **24**, 1868–1872.
- 55 C. Zhu, Y. Yang, M. Luo, C. Yang, J. Wu, L. Chen, G. Liu, T. Wen, J. Zhu and H. Xia, *Angew. Chem.*, 2015, **54**, 6181–6185.
- 56 C. Zhu, M. Luo, Q. Zhu, J. Zhu, P. V. Schleyer, J. I. Wu, X. Lu and H. Xia, *Nat. Commun.*, 2014, **5**, 3265.